HHS Public Access

Author manuscript

Nat Struct Mol Biol. Author manuscript; available in PMC 2016 April 07.

Published in final edited form as:

Nat Struct Mol Biol. 2015 September ; 22(9): 679–685. doi:10.1038/nsmb.3073.

Recognition of the bacterial alarmone ZMP through long-distance association of two RNA sub-domains

Christopher P. Jones and **Adrian R. Ferré-D'Amaré**

Biochemistry and Biophysics Center, National Heart, Lung and Blood Institute, National Institutes of Health, Bethesda, Maryland, USA

Abstract

The bacterial alarmone 5-aminoimidazole-4-carboxamide riboside 5'-triphosphate (ZTP), derived from the monophosphorylated purine precursor ZMP, accumulates during folate starvation. ZTP regulates genes involved in purine and folate metabolism through a cognate riboswitch. The linker connecting this riboswitch's two sub-domains varies in length by over 100 nucleotides. We report the co-crystal structure of the *Fusobacterium ulcerans* riboswitch bound to ZMP, which spans the two sub-domains whose interface also comprises a pseudoknot and ribose zipper. The riboswitch recognizes the carboxamide oxygen of ZMP through an unprecedented inner-sphere coordination with a Mg^{2+} ion. We demonstrate that the affinity of the riboswitch for ZMP is modulated by the linker length. Notably, ZMP can bind to the two sub-domains together even when synthesized as separate RNAs. The ZTP riboswitch demonstrates how specific small-molecule binding can drive association of distant non-coding RNA domains to regulate gene expression.

INTRODUCTION

Purine biosynthesis is an ancient metabolic pathway common to most organisms. Its final steps are the conversion of 5-amino-4-imidazolecarboxamide riboside 5'-monophosphate (AICAR or ZMP) into 5-formyl-AICAR (FAICAR), which is converted into inosine monophosphate, a precursor for AMP and GMP (reviewed in ref. 1). The bifunctional enzyme AICAR transformylase-IMP cyclohydrolase (PurHJ) catalyzes the formation of FAICAR from AICAR, using 10-formyl-tetrahydrofolate (10f-THF) as the formate source. During purine or folate starvation, cells accumulate ZMP or its triphosphate derivative (ZTP), which were proposed to act as "alarmones", or signals for metabolic stress due to low amounts of either precursor[2]. Tetrahydrofolate (THF) is essential for the synthesis of purines, pyrimidines, and some amino acids, so the detection of low THF levels is a critical check on the cellular metabolic state.

Correspondence should be addressed to A.R.F.-D. (adrian.ferre@nih.gov).

Accession codes. Protein Data Bank: Atomic coordinates and structure factor amplitudes for the *F. ulcerans* ZTP riboswitch in complex with ZMP have been deposited with accession code 5BTP.

AUTHOR CONTRIBUTIONS

C.P.J. designed and carried out experiments, data analysis, diffraction data collection, and structure determination. C.P.J. and A.R.F. prepared the manuscript.

Recently, a riboswitch within the *pfl* operon was found to be the cellular means for sensing accumulation of Z nucleotides[3]. ZMP and ZTP were shown to bind to a conserved non-coding element of *pfl* mRNA transcripts from various bacterial species that function as genetic "ON" switches—transcription-promoting riboswitches when bound to ZMP or ZTP. Riboswitches are gene-regulatory mRNA domains that directly sense the intracellular concentration of their cognate ligands and regulate gene expression in *cis*. They are a widespread mechanism of gene control throughout bacteria (reviewed in refs. 4–6). In cells deprived of purines or folate, Z nucleotide accumulation leads to the activation of riboswitch-controlled genes. These include enzymes involved in purine biosynthesis like PurHJ or in the folate cycle like pyruvate formate lyase (the namesake enzyme of the *pfl* operon), as well as other genes[3]. Both ZMP and ZTP bind the *pfl* riboswitch and likely both control riboswitch function *in vivo*[3].

The predicted secondary structure[3,7] of the ZTP riboswitch minimal ligand-binding (or "aptamer") domain consists of two sub-domains that associate through formation of a pseudoknot[8]. Phylogenetic comparison suggested that the sequence-variable linker that covalently connects the two sub-domains of the RNA can comprise from a few to over one hundred nucleotides[3,7]. Such an arrangement of constituent elements is unprecedented among structurally characterized riboswitches. Even the spatially distant Stem I and antiterminator domains of T-box riboswitches are typically connected by a highly structured linker[9]. To understand at the atomic level how ZMP controls gene expression through the *pfl* motif, we have now determined the crystal structure of the *F. ulcerans* ZTP riboswitch bound to ZMP at 2.8 Å resolution. Our structure reveals how distant non-coding RNA elements coalesce to form a single ZMP-binding pocket, and suggests a mechanism for ligand-dependent RNA pseudoknot stabilization. The linker connecting the two sub-domains of the RNA is crystallographically disordered. We have demonstrated biochemically that its length modulates thermodynamically the stability of the aptamer domain and kinetically the intrinsic efficiency of transcriptional read-through. Since ZMP connects folate metabolism and purine biosynthesis, understanding how Z nucleotides regulate *pfl* gene expression would inform the design of Z nucleotide-based antibiotics. Sulfonamides and trimethoprim act through the inhibition of folate-synthesizing enzymes (reviewed in ref. 10), and ZTP riboswitches may offer an alternative avenue for the development of specific antibacterial compounds.

RESULTS

Screening of ZTP riboswitches

Initial studies of the ZTP riboswitch were plagued by RNA misfolding[3]. To avoid poorly behaved RNAs, we screened riboswitch aptamer domains from eight bacterial species (Supplementary Fig. 1 and Supplementary Table 1) for ZMP binding using isothermal titration calorimetry (ITC). Some of these RNAs bound ZMP with μM to sub-μM apparent dissociation constants (K_D) (Supplementary Table 2), with the tightest binding RNAs from *Halothermothrix orenii* (K_D = 110 nM) and *F. ulcerans* (K_D = 487 nM). Several RNAs did not bind ZMP under the conditions tested (*i.e., Klebsiella pneumoniae, Paenibacillus sp. HGF5*, and *Spirochaeta thermophila*). RNAs competent for ZMP binding were screened for

co-crystallization with ZMP and, in the case of the *F. ulcerans* riboswitch, produced well-diffracting crystals (Supplementary Fig. 2a,b).

Overall structure of the *F. ulcerans* ZTP riboswitch

The co-crystal structure was solved by the single-wavelength anomalous dispersion (SAD) method using data from an iridium hexammine-soaked crystal[11]. The electron density maps were of excellent quality (Supplementary Fig. 2c) and allowed unambiguous chain tracing. The bound ZMP molecule was readily identified but was not included in the crystallographic model until the final stages of refinement. The structure has been refined against diffraction data extending to 2.8 Å resolution (Methods and Table 1) to a free-*R* value of 22.1%. Two near-identical copies of the RNA were present in the crystallographic asymmetric unit. While this manuscript was under review, structures of *Thermosinus carboxydivorans*[12] and *Actinomyces odontolyticus*[13] ZTP riboswitches were published. They are in general agreement with the structure reported here.

The ZTP riboswitch folds into a compact structure consisting of four helices (paired regions P1–P4) (Fig. 1). Two sub-domains associate through a pseudoknot (helix P4). Helices P1 and P2 form the 5' sub-domain of the RNA, while P3 and P4 form the 3' sub-domain (Fig. 1b). P1, P2, and P3 come together through formation of the pseudoknot helix P4 between the apical loop of P3 (nts 64–70) and the residues connecting helices P1 and P2 (nts 17–24). Sixty of the 75 residues of the crystallization construct are visible in our experimental electron density maps; residues at the 5' terminus and in the linker between helices P1 and P3 have no electron density and are presumed to be disordered (Fig. 1a,b). The riboswitch secondary structure agrees with sequence-based predictions[7], except for four base pairs in P1 formed between residues 13–16 and 40–43. These include two purine-purine pairs between conserved residues G13•A43 and A14•A42 and the U16•U40 pair (Fig. 1a). In-line probing experiments[3] suggested that these eight nucleotides are single-stranded in the absence of ZMP; their pairing may be part of the ligand-stabilized interactions responsible for the gene regulatory decision (Discussion).

ZMP binding site stitches together four helical elements

ZMP joins the cores of the two halves of the riboswitch, being recognized through interactions with residues adjacent to all four helical segments (Fig. 2). These interactions are distributed across three layers of highly conserved nucleotides that incorporate ZMP into a continuous helical stack from P3 into P4 (Fig. 2a). On the bottom layer, G63 and G71 stack on the Z nucleobase and ribose, respectively, and pair with each other through a single hydrogen bond. The 2'-OH of G63 also contributes a hydrogen bond to the 3'-OH of ZMP (Fig. 2a,c). Mutation of either G63 or G71 to A or U completely abolished ZMP binding as measured by ITC (Supplementary Table 2). In the middle layer, the Watson-Crick face of U70 interacts with the ZMP *via* two hydrogen bonds, which would not be provided by an A, G, or C at this position, consistent with the high phylogenetic conservation[3] of U70 and the complete loss of ZMP binding observed in the U70A and U70C mutants (Supplementary Table 2). The top layer is formed by the longest-range base pair in RNA, formed between the highly conserved[3] G17 and C69 (Fig. 2a). These two residues contribute three interactions to ZMP binding—a hydrogen bond from N7 of G17 to the 2'-OH of ZMP, a

hydrogen bond from N4 of C69 to the ZMP phosphate, and stacking interactions between G17 and the Z nucleobase. Mutation of the G17-C69 pair to either C17-G69 or A17-U69 also resulted in a complete loss in ZMP binding, as measured by ITC (Supplementary Table 2).

In addition to these interactions, the O6 carbonyl oxygen of the carboxamide moiety of ZMP makes an inner-sphere coordination to a highly ordered Mg^{2+} ion that brings all four helices together. This Mg^{2+} ion is also coordinated by non-bridging phosphate oxygen atoms from U16 (helix P1) and C35 (helix P2) (Fig. 2b). Each phosphate also contributes one hydrogen bond to N4 and carboxamide amino group N6 of ZMP, respectively. Two water molecules (W_A and W_B) coordinate the Mg^{2+} ion and form hydrogen bonds with O4' of G17 and the 2'-OH of G71, respectively (Fig. 2b). Together with U70, these interactions create a binding site that surrounds the Z nucleobase on three sides (Fig. 2c). Consistent with the importance of the inner-sphere coordination between this Mg^{2+} and ZMP, iridium hexammine (whose amino ligands are kinetically inert, and can thus participate only in outer-sphere coordination) did not bind appreciably at this site (not shown). Hydrogen bonds from the RNA contact the ZMP ribose and phosphate moieties; however the distal end of the phosphate of the alarmone points out into bulk solution, which is consistent with the observation that ZMP and ZTP bind the riboswitch similarly[3].

On the nucleobase side of the bound ZMP, the base of the highly conserved[3] A34 from loop L2 makes type I A-minor interactions[14] with the G17-C69 base pair (Fig. 2d,e), the same pair that contacts ZMP. The P2 helix is typically a 5-base pair stem with a loop of four or five residues[3], but in the *F. ulcerans* riboswitch, the stem is four base pairs with a six-residue AAUUAA loop L2. Interestingly, both of the tightest binding species of riboswitches examined, *F. ulcerans* and *H. orenii*, possess this loop sequence (Supplementary Fig. 1a). In the *F. ulcerans* RNA, mutating loop L2 residues 29–34 to either a U1A binding site, a GAAA tetraloop, or a UCUG tetraloop abolished ZMP binding, emphasizing its importance (Supplementary Table 2). In the *F. ulcerans* crystal structure, U32 is looped out, A33 stacks on A34, and A29 stacks on A30 (Fig. 2d). Both A29U and A33U mutations weaken ZMP binding, by ~56-fold and ~4-fold, respectively, while the A33G mutation (K_D = 599 nM) binds similarly to the wild-type RNA, consistent with stacking being its primary function. A34 is more than 90% conserved[3] among *pfl* species (Supplementary Fig. 3), suggesting that this tertiary contact is a feature shared among ZTP riboswitches even if the sequence and connectivity vary (Supplementary Fig. 1). Mutation of A34 to a U or G results in 69-fold (K_D = 33.5 μM) and 100-fold (K_D = 50.2 μM) weaker binding, respectively, relative to wild-type (Supplementary Table 2). A second tertiary contact within loop L2 occurs between A30 and the backbone of P4 in hydrogen bonds between N1 of A30 to the 2'-OH of A18 and N6 of A30 to the 3'-O of A18 (Supplementary Fig. 3).

ZMP binding stabilizes the *pfl* riboswitch

Although the three-dimensional structure of the ZTP riboswitch is relatively compact (153 $Å^2$ solvent-accessible surface per residue) when compared to other RNAs[15], its secondary structure suggests that the RNA is initially extended during transcription and folds in response to ZMP or ZTP binding. To investigate this biophysically, we purified the *F.*

ulcerans, H. orenii, and *T. carboxydivorans* riboswitches by size-exclusion chromatography (SEC, Supplementary Fig. 4a,b) and examined the effect of ligand by small-angle X-ray scattering (SAXS), which reports on the overall shape of a macromolecule in solution (reviewed in ref. 16).

In the absence of ZMP, SAXS analyses frequently indicated non-specific aggregation by the three RNAs. Aggregation results in increased, skewed scattering at low angles (Supplementary Fig. 4c), which compromises calculation of the radius of gyration (R_g) and end-to-end distance (D_{max}). For the *F. ulcerans* RNA, samples in the absence of ZMP that did not display overt aggregation were characterized by an R_g = 25.3 Å and D_{max} = 86 Å (Table 2). Notably, these samples still had ~25% larger Porod volumes (V_P) than ZMP-bound samples, suggesting that less severe aggregation or dimerization may still be occurring. Thus, the change in R_g between the bound and free states could reflect RNA-RNA association in addition to ligand binding. In the presence of ZMP, scattering curves showed no signs of aggregation (Supplementary Fig. 4c). All three ZMP-bound RNAs are compact in solution, with R_g ~ 21–24 Å and D_{max} ~75 Å (Table 2). These values are similar to those observed[17] for tRNAs, which are approximately the same size as the *pfl* RNAs examined herein. The Kratky plot portrays the compactness of a macromolecule[16] and changes in it can reflect global conformational changes in riboswitches[18]. Kratky plots of the *F. ulcerans* riboswitch in the presence and absence of ligand are practically identical, suggesting that after transcription and purification, the RNA may be globally prefolded (Supplementary Fig. 4d).

Common among the *pfl* riboswitch species examined is presence of dimeric or higher order species. In our crystals, a non-crystallographic dimer interface is observed between the two copies of *pfl* RNA in the asymmetric unit involving residues A23 and A64 (Fig. 2f), which are not highly conserved (Supplementary Fig. 3). A23 and A64 stack on the G21-C65 pair, and A23 nucleobases from each RNA stack on one another. The Watson-Crick face of A64 from one RNA hydrogen bonds to the sugar edge of A23 of the other RNA (Fig. 2f). Nearby residue A22 is involved in crystal packing and stacks with A22 from the adjacent dimer (Supplementary Fig. 4e). SEC peaks corresponding to the monomeric and dimeric *F. ulcerans* riboswitch were purified to test the contribution of each oligomeric state to ZMP binding (Supplementary Fig. 4f). Both oligomeric states bind ZMP with similar K_D of ~400 nM (Supplementary Table 2). SEC analysis of the ITC samples revealed that the dimer converts to monomer during the titration while the monomer remains monomeric (Supplementary Fig. 4f), indicating that the riboswitch functions as a monomer. Together, both SEC and SAXS results suggest that ZMP binding to *pfl* RNA prevents misfolding by stabilizing the monomeric state. The increased R_g and D_{max} observed by SAXS in the absence of ligand (Table 2) are likely due to varying amounts of dimerization, which is alleviated by addition of ZMP.

Linker length modulates ZMP affinity and antitermination

The aptamer domain of the ZTP riboswitch is composed of two sub-domains that associate through space by formation of the pseudoknot helix P4 and binding of ZMP or ZTP, but which can be separated by a linker of over 100 nt (Fig. 1). To examine the consequences of

the naturally observed variation in linker length, we tested ZMP binding by ITC to *F. ulcerans* riboswitch variants with either 10 or 20 adenosines inserted between residues 55 and 56 (Fig. 3). Additionally, we inserted a naturally occurring 102-nt linker from environmental sample 3278 (env3278, Fig. 3a and Supplementary Fig. 1h), which appears in a subset of *pfl* variants[3]. The K_D for ZMP is increased by ~6-fold for the 10A insertion (K_D = 2.99 μM), ~10-fold for the 20A insertion (K_D = 4.74 μM), and ~20-fold for the 102-nt insertion (K_D = 9.70 μM) (Supplementary Table 2 and Supplementary Fig. 5a–e). These observations suggest that increased linker length imposes an entropic penalty on folding of the RNA. To examine the effect of an arbitrarily long linker, we prepared an isolated 5' subdomain of the ZTP riboswitch (Δ55–75). This RNA did not bind ZMP by itself (Supplementary Table 2 and Supplementary Fig. 5f). However, when the 3' sub-domain (nts 59–75) was supplied in *trans*, the RNA bound ZMP with a dissociation constant even larger than that of the construct with the 102-nt linker (K_D = 15.2 μM). These experiments confirm that association of the two sub-domains is required for ZMP binding and, given that our SAXS data shows that the two sub-domains can associate prior to ZMP binding, imply that linker length modulates stability of the aptamer domain.

The naturally occurring variation in the linker connecting the riboswitch sub-domains may serve to modulate the threshold of ZMP required to activate gene expression, or to fine-tune riboswitch response to RNA polymerase elongation speed. The *Clostridium beijerinckii* ZTP riboswitch has been previously shown to function as a transcriptional "ON" switch by preventing the formation of a transcription termination hairpin in the ZMP-bound state[3]. In those experiments, the concentration of ZMP required to terminate transcription was much greater than the K_D determined from in-line probing, suggesting that the ZTP riboswitch is kinetically controlled[3]—that is, the speed of transcription by RNA polymerase is too fast for ligand binding to reach equilibrium[19].

The *F. ulcerans* ZTP riboswitch we have studied is also predicted to form a terminator hairpin in the "OFF" state, employing alternative base pairing of residues that form helices P3 and P4 in the "ON" (or antiterminator) state (Fig. 4a). To test the contribution of linker length to the transcriptional readout of the riboswitch, we examined the same linker variants as above in single-round transcription assays (Fig. 4 and Supplementary Fig. 5g) in the presence and absence of 0.1 mM ZMP (which was previously shown to be saturating for the *C. beijerinckii* ZTP riboswitch[3]). In the absence of ZMP, the wild-type riboswitch antiterminates 17% (Fig. 4b), while in the presence of ZMP, production of full-length RNA increased by 130% (Fig. 4c). For transcription assays with ZTP riboswitch linker variants, two effects were observed. First, for all three longer variants, more full-length RNA was produced in the absence of ZMP compared to the wild-type riboswitch (Fig. 4b). This enhancement in the basal level of transcription antitermination suggests that increased transit time of the polymerase through the longer linkers may allow more time for the P1 and P2 helices to fold (and thus increases their efficiency in "capturing" P3 and P4 as they are transcribed). Second, as the linker length separating the two sub-domains was increased, addition of ZMP resulted in progressively smaller relative enhancement of transcriptional antitermination (Fig. 4c). The reduction in the effect of ZMP is consistent with the progressively weaker binding (Supplementary Table 2 and Supplementary Fig. 5a–f) of the

small molecule resulting from decreased stability of the aptamer domain as linker length is increased.

DISCUSSION

Many of the metabolites recognized by naturally occurring riboswitches are purines, are purine-related, or contain purine moieties (reviewed in refs. 6,20). Atomistic structures have been reported for riboswitches that recognize simple purines[21,22], cyclic purine dinucleotides[23–29], S-adenosyl methionine[30–32], vitamin B12 (refs. 33,34), flavin mononucleotide[35], THF (refs. 36,37), and the hypermodified purine preQ$_1$ (refs. 38–41). The Mg^{2+}-mediated recognition of the ketone oxygen of the ZMP carboxamide moiety we have uncovered is thus far unique (Fig. 2b,c), but the residues forming the ZMP binding pocket share some similarity to those of other riboswitch ligand-binding sites. Ligand-Mg^{2+} coordination typically occurs at ligand phosphate groups, as in the FMN and TPP riboswitches[35,42–44]. Examples of coordination between carboxylate groups of bound amino acids and cations are seen in the glycine riboswitch[45,46] (with Mg^{2+}) and lysine riboswitch (with K^+)[47,48]. The guanine and THF riboswitches[21,22,36,37] both recognize purines using three hydrogen bonds between the Watson-Crick face of a U residue of the RNA and the minor groove face of guanine (Fig. 5a) or the guanine-like pterin ring of THF (Fig. 5b). The corresponding interaction between U70 and the Hoogsteen face of ZMP involves only two hydrogen bonds, one of which is donated by the carboxamide amino group N6 (Fig. 5c). Like the THF riboswitch, the ZTP riboswitch entirely surrounds the nucleobase moiety of its ligand while the opposite end of the molecule points into solution (Fig. 2), allowing for binding to both ZMP and ZTP. Both ZMP's biosynthetic precursor (succinyl-ZMP) and successors (e.g., FAICAR, inosine monophosphate, and purines) would be unable to bind the ZTP riboswitch due to steric clash with the phosphates and coordinated Mg^{2+}. Even the addition of a single methyl group to the carboxamide moiety of the Z nucleobase eliminates ligand binding[3].

Since the phosphate end of the bound ZMP is exposed to bulk solvent (Fig. 2), ZMP could enter a largely preformed binding site and stabilize the binding pocket after the pseudoknot has already folded. SAXS data show little to no global conformational change upon ZMP binding (Table 2), so the pseudoknot may form independently from ligand binding. This would be reminiscent of the FMN riboswitch, whose global structure was unaffected by ligand binding according to SAXS experiments[49] and enzymatic probing[35]. However, in-line probing of the *Clostridium bartletti* ZTP riboswitch suggests that helix P4 and four base pairs of P1 are less reactive upon ZMP binding[3]. These four pairs correspond to residues 13–16 and 40–43 in the *F. ulcerans* riboswitch, which, aside from U40, are highly conserved (Supplementary Fig. 3) and may constitute part of a ligand-dependent conformational switch. It is possible that SEC purification of the riboswitch prior to SAXS eliminated the flexibility and heterogeneity observed in probing experiments. Alternatively, while the overall shape of the riboswitch may be unchanged, the residues surrounding ligand binding site could be more flexible in the absence of ligand. In either case, formation of the pseudoknot helix is predicted to compete with the downstream transcription termination hairpin (Fig. 4a), so in the absence of ZMP the riboswitch aptamer domain must remain

plastic enough to unfold once the downstream terminator sequence has been fully transcribed.

Among the purine and purine-related riboswitches, many contain pseudoknots, but none have an internal segment as long and as variable as the linker separating the two sub-domains of the ZTP riboswitch. Engineering longer linkers weakens ZMP binding (Fig. 3, Supplementary Table 2), but an RNA with the longest known naturally-occurring linker binds to its ligand with dissociation constant comparable to that of a *trans*-acting (*i.e.*, split) riboswitch (Fig. 3). Riboswitches are thought to function through either kinetic or thermodynamic control depending on the competition between ligand binding and transcription termination that ultimately results in the gene control decision (reviewed in refs. 6,19). The longer linker variants of ZTP riboswitches often contain stem-loops, as exemplified by the *T. bispora* linker separating helices P4 and P2 (Supplementary Fig. 1e) and environmental sample 3278 linker separating helices P1 and P3 (Supplementary Fig. 1h). These stem-loops could serve as transcriptional pause sites that act to retard elongation and allowing the RNA more time to fold, thereby altering the mode of thermodynamic or kinetic control. Consistent with the two sub-domains of the riboswitch associating prior to ZMP binding, single-round transcription experiments (Fig. 4) imply that linker length primarily controls the antitermination efficiency of the *F. ulcerans* riboswitch in the absence of ZMP, rather than the dynamic range of the genetic switch.

Several examples of *trans*-acting riboswitches have been previously described[50–52]. In these cases, the *trans*-association is analogous to sRNA-target binding and is mediated by Watson-Crick base pairing. The *pfl* riboswitch is distinctly different in that the association of its two constituent sub-domains is ligand mediated, and, in addition to pseudoknot formation (by definition involving Watson-Crick base pairing[8]), other tertiary interactions are involved. We have demonstrated that the two sub-domains of the ZTP riboswitch can associate in *trans* to bind ZMP (Fig. 3). This opens the way to the design of split variants of the ZTP riboswitch that could in principle function in cells to coordinate the expression of two disjoint transcriptional units. Moreover, such ligand-mediated *trans*-association may underlie the function of as yet uncharacterized cellular non-coding RNAs.

ONLINE METHODS

Preparation of *pfl* riboswitch RNAs

RNAs were *in vitro* transcribed from DNA templates prepared by PCR from plasmids (Integrated DNA Technologies) encoding *pfl* cDNAs, and purified using denaturing polyacrylamide gel electrophoresis as previously described[53]. The insert of the *Fusobacterium ulcerans* wild-type plasmid pFulpfl is identical to GenBank ACDH02000027.1, nts 25274–25200 (antisense). The wild-type *pfl* plasmids from other bacterial species are described in Supplementary Table 1, as well as the *pfl* plasmid containing the 102-nt env3278 insertion sequence. Plasmids and DNA templates were designed to obtain homogeneous RNA 5' and 3' ends during transcription, as previously described[23]. Site-directed mutagenesis was performed using QuikChange kits (Agilent) with oligonucleotide primers (Integrated DNA Technologies). Prior to use, RNAs were brought up in a buffer containing 50 mM HEPES-KOH, pH 7.4 and 150 mM KCl, and heated at

80 °C for 2 min and 60 °C for 2 min. $MgCl_2$ was then added to 10 mM final concentration, and the solution was placed on ice for at least 30 min. For crystallization, *pfl* RNAs were folded in the presence of 1.25-fold excess ZMP (Sigma Aldrich).

Crystallization and diffraction data collection

Crystals were grown by hanging-drop vapor diffusion at 20°C by adding 1.4 μL of a 200 μM RNA solution containing 50 mM HEPES-KOH, pH 7.4, 150 mM KCl, 10 mM $MgCl_2$, and 250 μM ZMP to 0.7 μL of a reservoir solution containing 50 mM Bis-Tris-HCl, pH 8.0, 0.2 M $LiSO_4$, and 30% (w/v) polyethylene glycol (PEG) 4000, and equilibrated against 500 μL of reservoir solution. Crystals were grown with the less expensive ZMP rather than ZTP since both Z nucleotides bind to the riboswitch with near-equivalent affinity[54]. Hexagonal bipyramid-shaped crystals appeared within 2 days, and grew to maximum dimensions of 250 × 250 × 250 μm^3 over a week. Crystals primarily nucleated out of precipitate (Supplementary Fig. 2a). A single crystal was washed three times with stabilizing solution, and the washes and dissolved crystal were analyzed *via* denaturing polyacrylamide gel electrophoresis. Staining with ethidium bromide confirmed the presence of intact RNA in the crystal (Supplementary Fig. 2b). For heavy-atom derivative preparation, 1 μL of reservoir solution supplemented with 10 mM iridium (III) hexammine was added directly to the drops, which were then incubated for up to 3 hours at 20°C prior to vitrification in liquid nitrogen. Native and SAD data were collected at 1.0 Å and at the iridium L-III edge (1.105 Å), respectively, at 100 K at beamline 5.0.2 of the Advanced Light Source (ALS), Lawrence Berkeley National Laboratory. Data were integrated and scaled using the HKL (ref. 55) package.

Structure determination and refinement

The heavy atom substructure was determined with SHELX (ref. 56) and confirmed using HySS (ref. 57) implemented in Phenix (ref. 58). Phase-probability distributions were calculated using PHASER (ref. 59) with heavy atom sites from SHELX, and density-modified using RESOLVE (ref. 60) (Supplementary Fig. 2c). Satisfactory CC_{all}/CC_{weak} SHELXD scores were obtained for 9–15 iridium sites, but solutions for 11 iridium sites provided the best electron density maps. Manual model building was performed in Coot (ref. 61) with RCrane (ref. 62). Rounds of model building interspersed with refinement were then performed, using experimental phases and Ir-hexammine amplitudes until the free-R factor was 0.290. ZMP and coordinated Mg^{2+} and water ions were placed into the $|F_o|-|F_c|$ residual electron density (Fig. 2c), and final model building and refinement was performed against the native structure factor amplitudes, to a final free-R factor of 0.221. The mean coordinate precision of the crystallographic model is estimated[58] to be 0.37 Å. The average solvent-accessible surface area per residue was calculated over both copies of RNA in the asymmetric unit using StrucTools provided by Helix Systems at the National Institutes of Health, Bethesda, MD (http://helix.nih.gov).

Small-angle X-ray scattering

For SAXS experiments, 250 μL samples of 200 μM RNA (~5 g/L) were folded and purified by size-exclusion chromatography using a Superdex 200 Increase 10/300 GL column (GE). The column was equilibrated in a buffer matching the RNA folding conditions, and fractions

corresponding to the monomeric peak were concentrated by centrifugal ultrafiltration and stored for no more than 48 hours at 4°C until data collection at beamline 12-ID-C of the Advanced Photon Source (APS), Argonne National Laboratory. Samples of the RNAs were judged for final purity by native and denaturing polyacrylamide gel electrophoresis (Supplementary Fig. 4b). SAXS data were collected as previously described[63] on RNA samples at several concentrations (0.2–1 g/L) in the presence and absence of 100 μM ZMP. Data were analyzed as previously described[23].

Isothermal titration calorimetry

ITC measurements were made using a MicroCal iTC_{200} microcalorimeter (GE), and data were fit using NITPIC and SEDPHAT (refs. 64,65). All experiments were performed at 37 °C in RNA refolding buffer (50 mM HEPES-KOH, pH 7.4, 150 mM KCl, 10 mM $MgCl_2$). Typically, 20 μM RNA in the cell was titrated with 400 μM ZMP in the syringe, but higher concentrations of RNA were necessary for weaker binding RNAs. For examination of *F. ulcerans* Δ55–75 and 59–75 *in trans*, 40 μM of each RNA was folded together and titrated with 800 μM ZMP. For ITC experiments on SEC-purified RNA samples, ITC measurements were recorded first, and 100 μL of the ~300 μL cell solutions, which were bound to ZMP as judged by ITC, were used for post-ITC SEC analysis.

Single-round transcription termination assays

DNA templates containing a lambda phage promoter and 29-nucleotide C-less sequence[66] followed by the *F. ulcerans* ZTP riboswitch, termination hairpin, and downstream sequence (50 nts) were PCR amplified from wild-type and mutant plasmids (Supplementary Table 1) using primers described in Supplementary Table 3. Experiments were performed as previously described[54], with minor alterations. Halted transcription complexes were formed using a reaction mix containing 0.08 pmol μL^{-1} DNA template, 20 mM Tris-HCl, pH 8, 20 mM NaCl, 14 mM $MgCl_2$, 0.1 mM DTT, 0.1 mM EDTA, 1% glycerol, 130 μM ApU, 2.5 μM GTP, 2.5 μM UTP, 1 μM ATP, ~10 μCi ^{32}P-[α]-ATP, and 0.04 U μL^{-1} *E. coli* RNA polymerase holoenzyme (Epicenter), incubated at 37 °C for 10 min. Transcription was restarted by addition of 8 μL of halted complex to tubes containing 1 μL of 10× final concentration of ZMP and 1 μL of 150 μM ATP, 150 μM UTP, 150 μM GTP, 50 μM CTP, 1 mg mL^{-1} heparin, 20 mM Tris-HCl, pH 8, 20 mM NaCl, 14 mM $MgCl_2$, 0.1 mM DTT, 0.1 mM EDTA, and 1% glycerol. Transcription was allowed to proceed for 20 min at 37 °C. To remove DNA template, 1 μL of RNase-free DNase (Promega) was added, and the mixture was incubated at 37 °C for 30 min. 10 μL of loading dye (8 M urea, 20% sucrose, 0.1% SDS, 0.01% bromophenol blue, 0.01% xylene cyanol, 90 mM Tris-HCl, 90 mM borate, and 1 mM EDTA, pH 8) was added, and the mixture was separated by 8% denaturing PAGE (Supplementary Fig. 7). Band intensities were measured using ImageQuant software (GE), background corrected, and normalized to account for the amount of ^{32}P-[α]-ATP incorporated into each band. The amounts of ZMP-induced anti-terminated RNA were calculated by dividing the total anti-terminated RNA in the presence of ZMP by the amount of anti-terminated RNA in the absence of ZMP, minus 100%.

Supplementary Material

Refer to Web version on PubMed Central for supplementary material.

Acknowledgments

We thank the staff at beamlines 5.0.1 and 5.0.2 of the Advanced Light Source at Lawrence Berkeley National Laboratory for crystallographic data collection, R. Trachman for SAXS data collection, G. Piszczek (National Heart, Lung and Blood Institute, NHLBI, National Institutes of Health, NIH) for isothermal titration calorimetry support, and L. Fang, S. Seifert and X. Zuo at beamline 12-ID-C of the Advanced Photon Source, Argonne National Laboratory (ANL), for SAXS support. SAXS data were collected in a core facility of the Center for Cancer Research, National Cancer Institute (NCI) allocated under agreement between NCI and ANL (PUP-24152). We also thank S. Bachas, M. Chen, C. Fagan, M. Lau, R. Trachman, K. Warner, and J. Zhang for discussions. This work was partly conducted at the ALS on the Berkeley Center for Structural Biology beamlines, which are supported by the NIH. Use of ALS and APS was supported by the U.S. Department of Energy. This work was supported in part by the intramural program of the NHLBI, NIH, and a Lenfant Biomedical Fellowship to C.P.J.

REFERENCES

1. Hartman SC, Buchanan JM. Nucleic acids, purines, pyrimidines (nucleotide synthesis). Annu Rev Biochem. 1959; 28:365–410. [PubMed: 14400146]
2. Bochner BR, Ames BN. ZTP (5-amino 4-imidazole carboxamide riboside 5'-triphosphate): a proposed alarmone for 10-formyl-tetrahydrofolate deficiency. Cell. 1982; 29:929–937. [PubMed: 6185232]
3. Kim PB, Nelson JW, Breaker RR. An ancient riboswitch class in bacteria regulates purine biosynthesis and one-carbon metabolism. Mol Cell. 2015; 57:317–328. [PubMed: 25616067]
4. Peselis A, Serganov A. Themes and variations in riboswitch structure and function. Biochim Biophys Acta. 2014
5. Jones CP, Ferré-D'Amaré AR. RNA quaternary structure and global symmetry. Trends Biochem Sci. 2015; 40:211–220. [PubMed: 25778613]
6. Batey RT. Structure and mechanism of purine-binding riboswitches. Q Rev Biophys. 2012; 45:345–381. [PubMed: 22850604]
7. Weinberg Z, et al. Comparative genomics reveals 104 candidate structured RNAs from bacteria, archaea, and their metagenomes. Genome Biol. 2010; 11:R31. [PubMed: 20230605]
8. Pleij CW, Rietveld K, Bosch L. A new principle of RNA folding based on pseudoknotting. Nucleic Acids Res. 1985; 13:1717–1731. [PubMed: 4000943]
9. Zhang J, Ferré-D'Amaré AR. Structure and mechanism of the T-box riboswitches. Wiley Interdiscip Rev RNA. 2015
10. Kompis IM, Islam K, Then RL. DNA and RNA synthesis: antifolates. Chem Rev. 2005; 105:593–620. [PubMed: 15700958]
11. Keel AY, Rambo RP, Batey RT, Kieft JS. A general strategy to solve the phase problem in RNA crystallography. Structure. 2007; 15:761–772. [PubMed: 17637337]
12. Ren A, Rajashankar KR, Patel DJ. Global RNA Fold and Molecular Recognition for a pfl Riboswitch Bound to ZMP, a Master Regulator of One-Carbon Metabolism. Structure. 2015
13. Trausch JJ, Marcano-Velazquez JG, Matyjasik MM, Batey RT. Metal Ion-Mediated Nucleobase Recognition by the ZTP Riboswitch. Chem Biol. 2015
14. Nissen P, Ippolito JA, Ban N, Moore PB, Steitz TA. RNA tertiary interactions in the large ribosomal subunit: the A-minor motif. Proc Natl Acad Sci U S A. 2001; 98:4899–4903. [PubMed: 11296253]
15. Ferré-D'Amaré AR, Doudna JA. RNA folds: insights from recent crystal structures. Annu Rev Biophys Biomol Struct. 1999; 28:57–73. [PubMed: 10410795]
16. Putnam CD, Hammel M, Hura GL, Tainer JA. X-ray solution scattering (SAXS) combined with crystallography and computation: defining accurate macromolecular structures, conformations and assemblies in solution. Q Rev Biophys. 2007; 40:191–285. [PubMed: 18078545]

17. Rambo RP, Tainer JA. Improving small-angle X-ray scattering data for structural analyses of the RNA world. RNA. 2010; 16:638–646. [PubMed: 20106957]
18. Zhang J, Jones CP, Ferré-D'Amaré AR. Global analysis of riboswitches by small-angle X-ray scattering and calorimetry. Biochim Biophys Acta. 2014
19. Zhang J, Lau MW, Ferré-D'Amaré AR. Ribozymes and riboswitches: modulation of RNA function by small molecules. Biochemistry. 2010; 49:9123–9131. [PubMed: 20931966]
20. Serganov A, Patel DJ. Molecular recognition and function of riboswitches. Curr Opin Struct Biol. 2012; 22:279–286. [PubMed: 22579413]
21. Batey RT, Gilbert SD, Montange RK. Structure of a natural guanine-responsive riboswitch complexed with the metabolite hypoxanthine. Nature. 2004; 432:411–415. [PubMed: 15549109]
22. Serganov A, et al. Structural basis for discriminative regulation of gene expression by adenine- and guanine-sensing mRNAs. Chem Biol. 2004; 11:1729–1741. [PubMed: 15610857]
23. Jones CP, Ferré-D'Amaré AR. Crystal structure of a c-di-AMP riboswitch reveals an internally pseudo-dimeric RNA. EMBO J. 2014
24. Ren A, Patel DJ. c-di-AMP binds the ydaO riboswitch in two pseudo-symmetry-related pockets. Nat Chem Biol. 2014; 10:780–786. [PubMed: 25086509]
25. Gao A, Serganov A. Structural insights into recognition of c-di-AMP by the ydaO riboswitch. Nat Chem Biol. 2014; 10:787–792. [PubMed: 25086507]
26. Ren A, et al. Structural Basis for Molecular Discrimination by a 3',3'-cGAMP Sensing Riboswitch. Cell Rep. 2015; 11:1–12. [PubMed: 25818298]
27. Kulshina N, Baird NJ, Ferré-D'Amaré AR. Recognition of the bacterial second messenger cyclic diguanylate by its cognate riboswitch. Nat Struct Mol Biol. 2009; 16:1212–1217. [PubMed: 19898478]
28. Smith KD, et al. Structural basis of ligand binding by a c-di-GMP riboswitch. Nat Struct Mol Biol. 2009; 16:1218–1223. [PubMed: 19898477]
29. Smith KD, Shanahan CA, Moore EL, Simon AC, Strobel SA. Structural basis of differential ligand recognition by two classes of bis-(3'–5')-cyclic dimeric guanosine monophosphate-binding riboswitches. Proc Natl Acad Sci U S A. 2011; 108:7757–7762. [PubMed: 21518891]
30. Montange RK, Batey RT. Structure of the S-adenosylmethionine riboswitch regulatory mRNA element. Nature. 2006; 441:1172–1175. [PubMed: 16810258]
31. Gilbert SD, Rambo RP, Van Tyne D, Batey RT. Structure of the SAM-II riboswitch bound to S-adenosylmethionine. Nat Struct Mol Biol. 2008; 15:177–182. [PubMed: 18204466]
32. Lu C, et al. Crystal structures of the SAM-III/S(MK) riboswitch reveal the SAM-dependent translation inhibition mechanism. Nat Struct Mol Biol. 2008; 15:1076–1083. [PubMed: 18806797]
33. Johnson JE Jr, Reyes FE, Polaski JT, Batey RT. B12 cofactors directly stabilize an mRNA regulatory switch. Nature. 2012; 492:133–137. [PubMed: 23064232]
34. Peselis A, Serganov A. Structural insights into ligand binding and gene expression control by an adenosylcobalamin riboswitch. Nat Struct Mol Biol. 2012; 19:1182–1184. [PubMed: 23064646]
35. Serganov A, Huang L, Patel DJ. Coenzyme recognition and gene regulation by a flavin mononucleotide riboswitch. Nature. 2009; 458:233–237. [PubMed: 19169240]
36. Trausch JJ, Ceres P, Reyes FE, Batey RT. The structure of a tetrahydrofolate-sensing riboswitch reveals two ligand binding sites in a single aptamer. Structure. 2011; 19:1413–1423. [PubMed: 21906956]
37. Huang L, Ishibe-Murakami S, Patel DJ, Serganov A. Long-range pseudoknot interactions dictate the regulatory response in the tetrahydrofolate riboswitch. Proc Natl Acad Sci U S A. 2011; 108:14801–14806. [PubMed: 21873197]
38. Klein DJ, Edwards TE, Ferré-D'Amaré AR. Cocrystal structure of a class I preQ1 riboswitch reveals a pseudoknot recognizing an essential hypermodified nucleobase. Nat Struct Mol Biol. 2009; 16:343–344. [PubMed: 19234468]
39. Liberman JA, Salim M, Krucinska J, Wedekind JE. Structure of a class II preQ1 riboswitch reveals ligand recognition by a new fold. Nat Chem Biol. 2013; 9:353–355. [PubMed: 23584677]
40. Kang M, Peterson R, Feigon J. Structural Insights into riboswitch control of the biosynthesis of queuosine, a modified nucleotide found in the anticodon of tRNA. Mol Cell. 2010; 39:653–655.

41. Spitale RC, Torelli AT, Krucinska J, Bandarian V, Wedekind JE. The structural basis for recognition of the PreQ0 metabolite by an unusually small riboswitch aptamer domain. J Biol Chem. 2009; 284:11012–11016. [PubMed: 19261617]
42. Serganov A, Polonskaia A, Phan AT, Breaker RR, Patel DJ. Structural basis for gene regulation by a thiamine pyrophosphate-sensing riboswitch. Nature. 2006; 441:1167–1171. [PubMed: 16728979]
43. Thore S, Leibundgut M, Ban N. Structure of the eukaryotic thiamine pyrophosphate riboswitch with its regulatory ligand. Science. 2006; 312:1208–1211. [PubMed: 16675665]
44. Edwards TE, Ferré-D'Amaré AR. Crystal structures of the thi-box riboswitch bound to thiamine pyrophosphate analogs reveal adaptive RNA-small molecule recognition. Structure. 2006; 14:1459–1468. [PubMed: 16962976]
45. Butler EB, Xiong Y, Wang J, Strobel SA. Structural basis of cooperative ligand binding by the glycine riboswitch. Chem Biol. 2011; 18:293–298. [PubMed: 21439473]
46. Huang L, Serganov A, Patel DJ. Structural insights into ligand recognition by a sensing domain of the cooperative glycine riboswitch. Mol Cell. 2010; 40:774–786. [PubMed: 21145485]
47. Serganov A, Huang L, Patel DJ. Structural insights into amino acid binding and gene control by a lysine riboswitch. Nature. 2008; 455:1263–1267. [PubMed: 18784651]
48. Garst AD, Heroux A, Rambo RP, Batey RT. Crystal structure of the lysine riboswitch regulatory mRNA element. J Biol Chem. 2008; 283:22347–22351. [PubMed: 18593706]
49. Baird NJ, Ferré-D'Amaré AR. Idiosyncratically tuned switching behavior of riboswitch aptamer domains revealed by comparative small-angle X-ray scattering analysis. RNA. 2010; 16:598–609. [PubMed: 20106958]
50. Mellin JR, et al. Riboswitches. Sequestration of a two-component response regulator by a riboswitch-regulated noncoding RNA. Science. 2014; 345:940–943. [PubMed: 25146292]
51. DebRoy S, et al. Riboswitches. A riboswitch-containing sRNA controls gene expression by sequestration of a response regulator. Science. 2014; 345:937–940. [PubMed: 25146291]
52. Loh E, et al. A trans-acting riboswitch controls expression of the virulence regulator PrfA in Listeria monocytogenes. Cell. 2009; 139:770–779. [PubMed: 19914169]

References

53. Xiao H, Edwards TE, Ferré-D'Amaré AR. Structural basis for specific, high-affinity tetracycline binding by an in vitro evolved aptamer and artificial riboswitch. Chem Biol. 2008; 15:1125–1137. [PubMed: 18940672]
54. Kim PB, Nelson JW, Breaker RR. An ancient riboswitch class in bacteria regulates purine biosynthesis and one-carbon metabolism. Mol Cell. 2015; 57:317–328. [PubMed: 25616067]
55. Otwinowski Z, Minor W. Processing of X-ray diffraction data collected in oscillation mode. Methods Enzymol. 1997; 276:307–326.
56. Schneider TR, Sheldrick GM. Substructure solution with SHELXD. Acta Crystallogr D Biol Crystallogr. 2002; 58:1772–1779. [PubMed: 12351820]
57. Grosse-Kunstleve RW, Adams PD. Substructure search procedures for macromolecular structures. Acta Crystallogr D Biol Crystallogr. 2003; 59:1966–1973. [PubMed: 14573951]
58. Adams PD, et al. PHENIX: a comprehensive Python-based system for macromolecular structure solution. Acta Crystallogr D Biol Crystallogr. 2010; 66:213–221. [PubMed: 20124702]
59. McCoy AJ, et al. Phaser crystallographic software. J Appl Crystallogr. 2007; 40:658–674. [PubMed: 19461840]
60. Terwilliger TC. Maximum-likelihood density modification. Acta Crystallogr D Biol Crystallogr. 2000; 56:965–972. [PubMed: 10944333]
61. Emsley P, Cowtan K. Coot: model-building tools for molecular graphics. Acta Crystallogr D Biol Crystallogr. 2004; 60:2126–2132. [PubMed: 15572765]
62. Keating KS, Pyle AM. RCrane: semi-automated RNA model building. Acta Crystallogr D Biol Crystallogr. 2012; 68:985–995. [PubMed: 22868764]

63. Baird NJ, Ferré-D'Amaré AR. Modulation of quaternary structure and enhancement of ligand binding by the K-turn of tandem glycine riboswitches. RNA. 2013; 19:167–176. [PubMed: 23249744]

64. Keller S, et al. High-precision isothermal titration calorimetry with automated peak-shape analysis. Anal Chem. 2012; 84:5066–5073. [PubMed: 22530732]

65. Schuck P. Size-distribution analysis of macromolecules by sedimentation velocity ultracentrifugation and lamm equation modeling. Biophys J. 2000; 78:1606–1619. [PubMed: 10692345]

66. Artsimovitch I, Henkin TM. In vitro approaches to analysis of transcription termination. Methods. 2009; 47:37–43. [PubMed: 18948199]

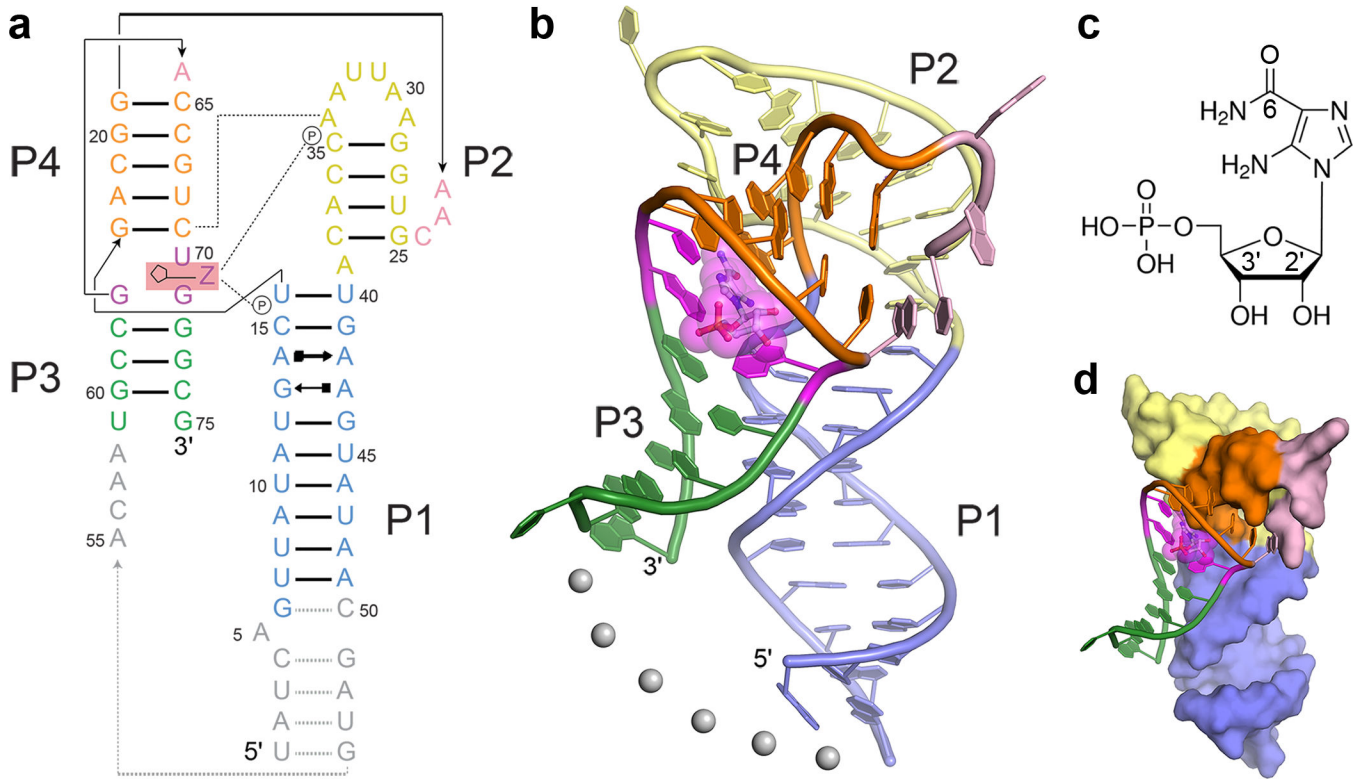

Figure 1.

Structure of the *F. ulcerans* ZTP riboswitch. (**a**) Secondary structure of the riboswitch based on the crystal structure. Paired regions P1 (blue), P2 (yellow), P3 (green), and pseudoknot helix P4 (orange) are labeled. Residues disordered in the crystal structure are in gray. The bound ZMP is boxed in magenta and indicated by a "Z" with nearby interacting residues G63, U70, and G71 colored magenta. Residues participating in dimerization and crystal contacts are colored pink. Lines with arrowheads indicate chain connectivity (gray line denotes crystallographic disorder). Dotted lines indicate interactions between ZMP and phosphates (U16 and C35) and A-minor interactions between A34 and the G17-C69 base pair. (**b**) Cartoon representation of the crystal structure of the ZTP riboswitch, colored as in A. Gray spheres denote the break in the crystallographic model at the disordered linker. (**c**) Chemical structure of ZMP; key atoms numbered (*i.e.*, carboxamide carbon labeled "6"). (**d**) Cartoon representation of the ZTP riboswitch crystal structure, colored as in A, emphasizing association of sub-domain 1 (sticks) and sub-domain 2 (surface).

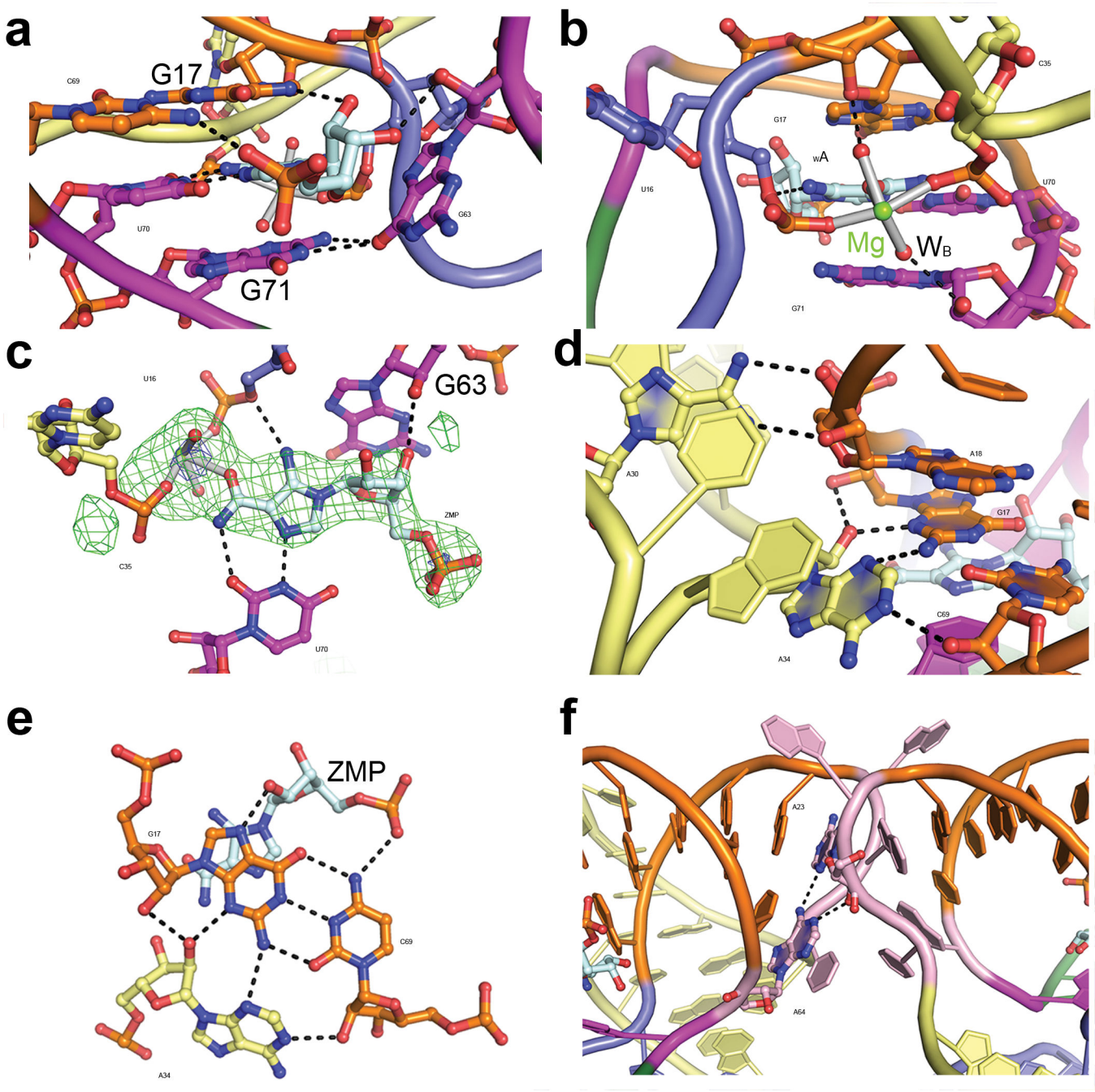

Figure 2.

Critical ligand-RNA and RNA-RNA interactions in the ZTP riboswitch. (**a**) Phosphate-side view of the bound ZMP with hydrogen bonds indicated by black dashed lines. The G17-C69 (orange) and G71•G63 (magenta) base pairs are above and below ZMP, respectively. The Watson-Crick face of U70 (magenta) contacts ZMP. (**b**) Nucleobase-side view of the bound ZMP, showing the critical Mg^{2+} ion (green) and two coordinated waters W_A and W_B. The Mg^{2+} also coordinates to the O4 carbonyl oxygen of ZMP, the phosphate of C35 (yellow), and the phosphate of U16 (blue). (**c**) View of the ZMP binding site in the plane of the ligand.

$|F_o|-|F_c|$ residual electron density map prior to ligand placement is shown, contoured at 3.0 and 7.5 σ (green and blue mesh, respectively). (**d**) Tertiary interactions between loop L2 residues A30 and A34 (yellow) with helix P4 residue A18 and the G17-C69 pair, respectively. (**e**) View of the interactions of the G17-C69 pair with ZMP and A34. (**f**) View of the two copies of RNA in the crystallographic asymmetric unit, which interact *via* residues A23 and A64 (pink).

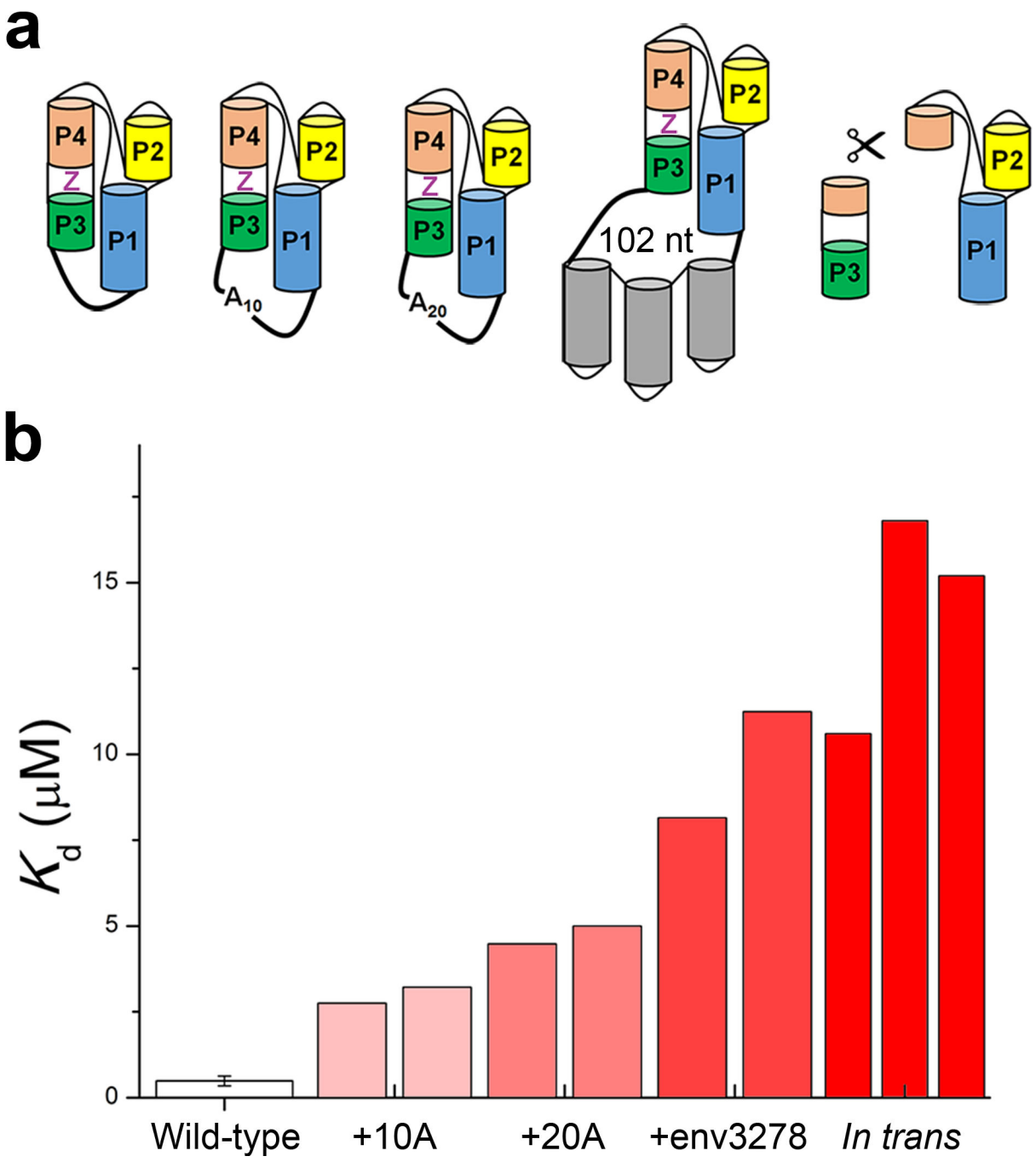

Figure 3.

Effect of linker length on ZMP binding affinity. (**a**) Cartoons of *F. ulcerans* riboswitches with varying linker lengths for the wild-type *F. ulcerans*, +10 adenosine linker, +20 adenosine linker, +102-nt linker derived from environmental sample 3278, and Δ55–75 plus 59–75 *in trans*. (**b**) Apparent dissociation constants (K_D) of riboswitch linker variants from isothermal titration calorimetric analysis. For wild-type ZTP riboswitch (n = 5), the average is shown, with s.d. For other experiments (n = 2 or 3), all independent experiments are shown.

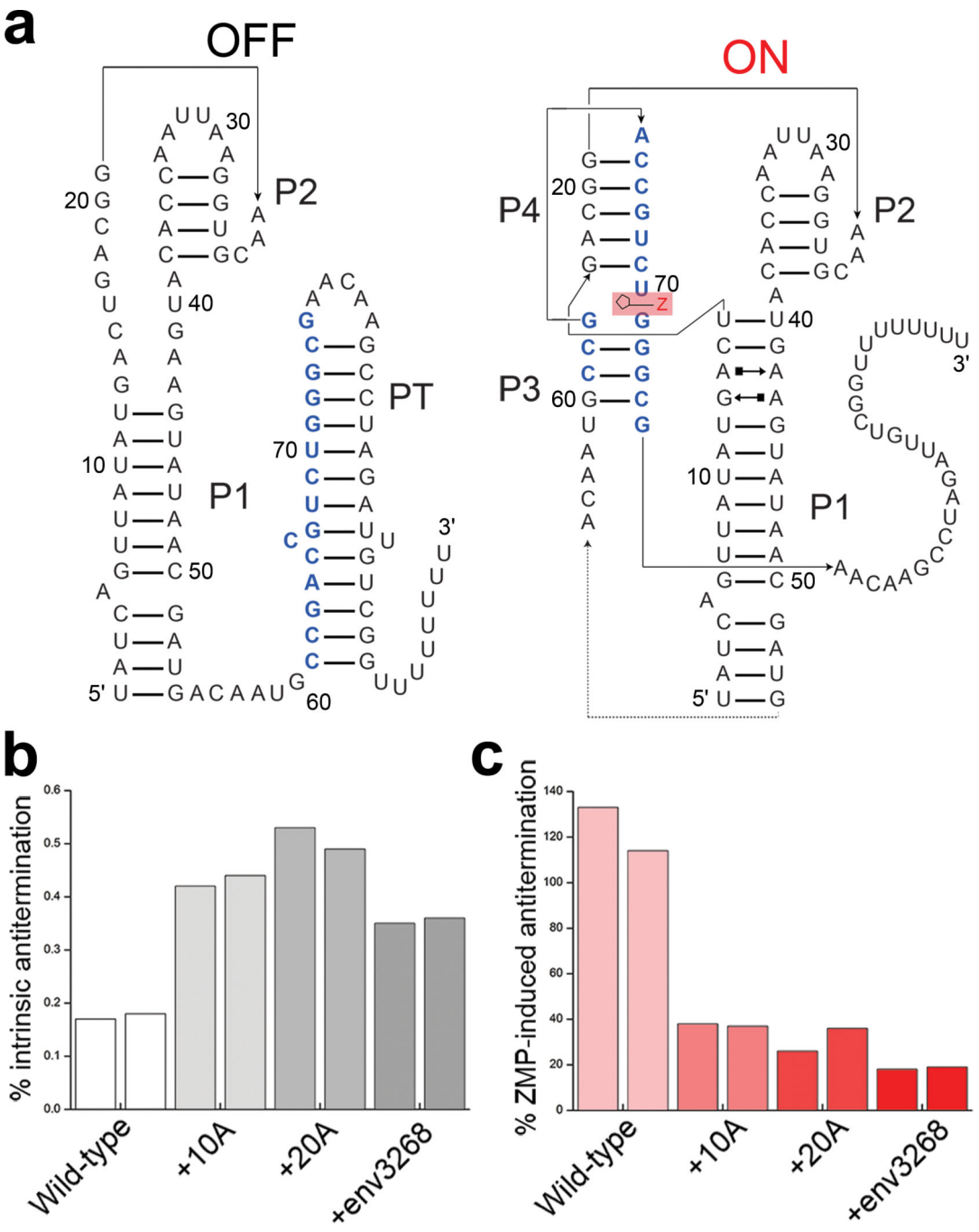

Figure 4.

Transcription antitermination by ZTP riboswitch linker variants. (**a**) Predicted secondary structures of the two states of the *F. ulcerans* ZTP riboswitch. "PT" denotes transcription terminator hairpin predicted to form in the "OFF" state in the absence of ZMP. Nucleotides within the terminator hairpin PT involved in alternative base pairing in helices P3 and P4 are colored blue. (**b**) Fraction of antiterminated RNA transcribed in the absence ZMP, as observed in single-round transcription assays. (**c**) Fractional increase of antiterminated RNA

induced by the presence of 0.1 mM ZMP. For all experiments, n = 2. Both independent experiments are shown for each linker variant.

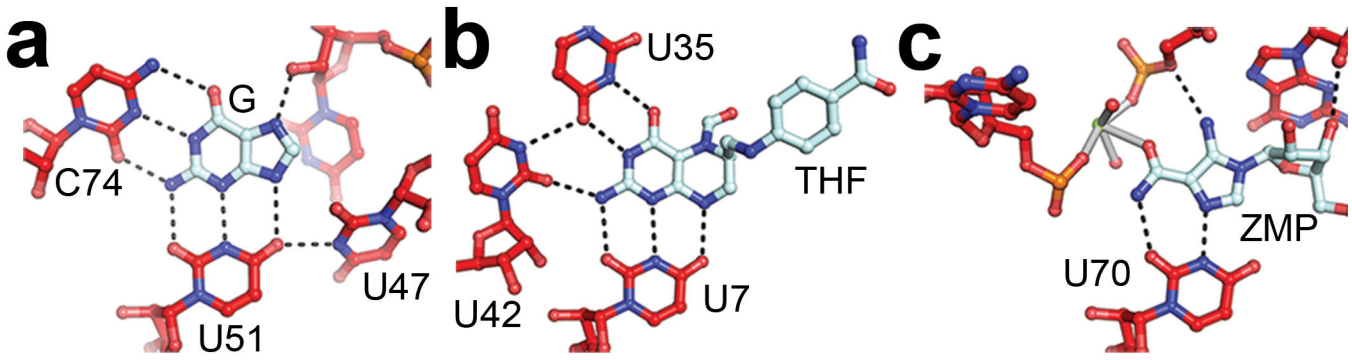

Figure 5.

Ligand recognition by purine and purine-like riboswitches. (**a**) Ligand binding site of the guanine riboswitch[22] bound to guanine (G). (**b**) Ligand binding site at the pseudoknot region of the THF riboswitch[36]. (**c**) Ligand binding site of the *F. ulcerans* ZTP riboswitch.

Table 1

Data collection, phasing and refinement statistics

	Native	**Ir-Hexammine**
Data collection		
Space group	$P3_221$	$P3_221$
Cell dimensions		
a, b, c (Å)	92.7, 92.7, 121.2	92.4, 92.4, 121.5
α, β, γ (°)	90, 90, 120	90, 90, 120
Resolution (Å)	30.3-2.82 (2.92-2.82)[a]	48.3-3.00 (3.05-3.00)[a]
R_{merge}	0.114 (1.78)	0.126 (1.00)
$I / \sigma I$	26.05 (1.79)	27.4 (0.62)
Completeness (%)	99.5 (96.2)	98.7 (87.0)
Redundancy	10.3 (10.9)	20.1 (14.7)
Refinement		
Resolution (Å)	30.3-2.82 (2.92-2.82)	
No. reflections	14947 (1404)	
R_{work} / R_{free}	0.186 / 0.221	
No. atoms		
RNA	2653	
ZMP	44	
Ions/water	20	
B factors		
Protein	106.9	
ZMP	73.1	
Ions/water	77.9	
r.m.s. deviations		
Bond lengths (Å)	0.002	
Bond angles (°)	0.829	

[a]Values in parentheses are for highest-resolution shell. Diffraction was collected from a single crystal for each dataset.

Table 2

Small-angle X-ray scattering analysis of ZTP riboswitches

RNA	R_g, Å	D_{max}, Å	V_P, Å^3
F. ulcerans	25.3	85.8	26300
F. ulcerans + ZMP	22.1	72.8	21100
H. orenii	_[a]	-	-
H. orenii + ZMP	24.1	77.0	30000
T. carboxydivorans	_[a]	-	-
T. carboxydivorans + ZMP	20.8	72.9	31200

[a]Calculations of R_g, D_{max}, and V_P were not possible due to aggregation.